Journal of
Instrumentation

PAPER • OPEN ACCESS

Experimental characterization and Monte Carlo validation of a GAGG/SiPM gamma camera prototype for ^{111}Ag imaging

To cite this article: E. Borciani *et al* 2026 *JINST* **21** P10036

View the article online for updates and enhancements.

You may also like

- Adsorption, manipulation and self-assembling of TBrPP-Co molecules on a Ag/Si(111) surface by scanning tunnelling microscopy
Qing Li, Shiro Yamazaki, Toyoaki Eguchi et al.
- Evaluation of irradiation effects on the microstructure and properties of Ag-sheathed Bi-2212 superconducting round wire for future application in CFETR
Zuoguang Li, Hongmei Zhu, Changjun Qiu et al.
- Assessment of the impact of the nuclear properties of -emitting radionuclides on the dosimetry of two radiopharmaceuticals with distinct pharmacokinetics
Laura De Nardo, Samuele De Zan, Kevin J H Allen et al.

This content was downloaded from IP address 62.205.16.30 on 26/10/2026 at 20:22

Published by IOP Publishing for Sissa Medialab

Received: *May 19, 2026*
Revised: *September 2, 2026*
Accepted: *September 27, 2026*
Published: *October 26, 2026*

Experimental characterization and Monte Carlo validation of a GAGG/SiPM gamma camera prototype for ^{111}Ag imaging

E. Borciani[a,b,c,*] **D. Serafini**[d,e,*] **G. Baldazzi**[a,b,c] **C. Sbarra**[a] **M. Negrini**[a] **A. Margotti**[a] **S. Spadano**[b] **G. Giannaccini**[b] **N. Lanconelli**[b] **G. Grosso**[f,g] **A. Gandini**[g,h] **E. Mariotti**[e,i] **and A. Andrighetto**[d]

[a] *INFN-Bologna, Viale C. Berti Pichat, 6/2, 40127 Bologna, Italy*
[b] *Università di Bologna, Viale Carlo Berti Pichat, 6/2, 40127 Bologna, Italy*
[c] *INAF/OAS, Via Piero Gobetti 93/3, 40129 Bologna, Italy*
[d] *INFN-Laboratori Nazionali di Legnaro, Viale dell'Università, 2, 35020 Legnaro PD, Italy*
[e] *University of Siena, Via Roma 56, 53100 Siena, Italy*
[f] *Department of Chemical Sciences, University of Padova, Padova, Italy*
[g] *Applied Nuclear Energy Laboratory (LENA), University of Pavia, Pavia, Italy*
[h] *Pavia Division, INFN, Pavia, Italy*
[i] *INFN-Pisa, Largo Bruno Pontecorvo 3, 56127 Pisa, Italy*

E-mail: borciani@infn.it, davide.serafini@lnl.infn.it

Abstract: A compact gamma camera prototype has been developed within the Isotope Separation On-Line production of radioPHARMaceutical (ISOLPHARM)–Advanced Dosimetry Methods and In-vitro Radiobiology of ^{111}Ag Labeled radiopharmaceuticals (ADMIRAL) project to enable laboratory studies and small animal imaging applications of the theranostic radionuclide ^{111}Ag, whose main gamma emission at 342 keV is above the energy range of conventional clinical systems, optimized for ^{99m}Tc.

The detector consists of a square-holes tungsten collimator facing a 23×23 pixelated GAGG(Ce) scintillator array optically coupled to an 8×8 Hamamatsu SiPM matrix and read out by a CAEN FERS (A5202) board, based on CITIROC 1A ASICs. A Geant4-based Monte Carlo application, including optical photon transport and an electronics-noise model, was developed and validated through laboratory measurements.

The prototype was characterized using a ^{133}Ba point-source-like and ^{111}Ag extended sources.

For ^{111}Ag, an energy resolution of $\Delta E/E \approx 24\,\%$ was observed at the 342 keV photopeak. Spatial resolution was assessed to be approximately 3 mm, in agreement with expectations from the Monte Carlo simulation.

*Corresponding author.

© 2026 The Author(s). Published by IOP Publishing Ltd on behalf of Sissa Medialab. Original content from this work may be used under the terms of the Creative Commons Attribution 4.0 licence. Any further distribution of this work must maintain attribution to the author(s) and the title of the work, journal citation and DOI.

https://doi.org/10.1088/1748-0221/21/10/P10036

2026 JINST 21 P10036

The efficiency of the camera on the γ-spectrum of ^{111}Ag was measured to be 2.1×10^{-4}. Finally, a preliminary mouse phantom study featuring multiple active regions confirmed the capability to qualitatively localize multiple activity regions.

These results demonstrate the feasibility of a prototype modular gamma camera, built using off-the-shelf components, for high-energy imaging of ^{111}Ag and provide an experimental platform for future optimization of collimation and reconstruction techniques.

KEYWORDS: Gamma camera, SPECT, PET PET/CT, coronary CT angiography (CTA); Gamma detectors (scintillators, CZT, HPGe, HgI etc); Photon detectors for UV, visible and IR photons (solid-state); Scintillators, scintillation and light emission processes (solid, gas and liquid scintillators)

2026 JINST 21 P10036

Contents

1 Introduction **1**

2 Material **2**

2.1 Device description 2

2.2 Front-end electronics structure 4

2.3 Pulse shape analysis 5

2.4 Equalization of SiPM array 6

2.5 Monte Carlo simulations 9

2.6 γ sources 11

2.7 Data collection and analysis 11

3 Results **13**

3.1 Flood field with ^{133}Ba 13

3.2 Spectroscopic response 14

3.3 System efficiency 16

3.4 Spatial response and imaging performance 17

3.5 Preliminary phantom imaging 20

3.6 Spatial linearity and resolution accuracy 20

3.7 Discussion 22

4 Conclusion **22**

1 Introduction

Targeted Radionuclide Therapy (TRT) is a technique used for cancer treatment, delivering a continuous low-dose-rate irradiation directly to tumor sites by binding radionuclides to molecular targeting vectors. Radionuclides emitting more than one type of radiation can provide an effective treatment that can be monitored externally. This gave rise to the concept of "Theranostics" to express the idea that the same radionuclide could be therapeutic as well as diagnostic [1]. TRT has unique promise as a vehicle for personalized cancer treatment, because both the targeting vehicle and the radionuclide can be tailored to the individual patient [2].

Radionuclides are currently produced in cyclotrons or nuclear reactors, which presents several limitations, such as the high costs of enriched targets, low reaction cross sections, and complex chemical separation routes. In addition, the specific activity, defined as the ratio between the radioactivity of the isotope and the mass of the radionuclide (MBq/mg), is generally very low in reactor production. This represents a significant challenge, since a high specific activity is essential for both therapeutic and diagnostic applications [3]. To address this problem, the Isotope Separation On-Line production of radioPHARMaceutical (ISOLPHARM) project [4] plans to use the Selective Production of Exotic Species (SPES) facility at Istituto Nazionale di Fisica Nucleare — Laboratori Nazionali di Legnaro to produce radionuclides of medical interest. One of the most promising candidates is ^{111}Ag, which emits both beta particles and γ rays [5]. ^{111}Ag has a half-life of 7.45 days and emits gamma lines at 342 keV ($\sim$ 7 %) and 245 keV ($\sim$ 1 %). These energies significantly exceed the 140 keV standard for which clinical gamma cameras are designed, typically optimized for ^{99m}Tc, and require a different optimization of the gamma camera parameters to maintain adequate detection efficiency and spatial resolution [5].

2026 JINST 21 P10036

Gamma cameras are usually composed of a tungsten/lead collimator, a scintillator crystal such as Sodium Iodide (NaI), a photodetector (photomultipliers tubes i.e. PMTs), all shielded by a thick layer of lead ($\sim$ 1–3 cm) [6]. The NaI crystal, PMTs and electronics can estimate the location of an interaction between a γ-ray and the crystal to within 3–4 mm of intrinsic spatial resolution, and energy resolution of $\sim$ 9–11 % at 140 keV, with a collimator length from 8 to 12 mm [7]. Reducing weight, volume, and cost while introducing modular architectures has become an important objective in the development of modern gamma cameras, to achieve more flexible operations [8].

Photomultiplier tubes suffer from several limitations, including large size, high operating voltages, fragility, and sensitivity to magnetic fields. In recent years, Silicon Photomultipliers (SiPMs) have emerged as a promising alternative due to their compactness and insensitivity to magnetic fields. SiPM arrays can have a wide dynamic range of linear response, high gain, low-voltage operation ($<$ 80 V), robustness, compact design and excellent timing performances (below 200 ps). Recent SiPMs achieve high values of photon detection efficiency (PDE $\sim$ 40 % at 520 nm), and have lower cost than PMTs [9–15]. Moreover, SiPM arrays can be integrated into high-density tiles, enabling modular high-resolution detection systems for spectroscopy and imaging. However, the leakage current, the possible cross-talk and after-pulse events that increase with bias voltage, and a nonlinear output at high photon rates, can be critical issues in photo-detection applications [9, 15].

Cerium-doped Gadolinium Aluminum Gallium Garnet (GAGG(Ce)) has emerged as a robust alternative to NaI(Tl) and LYSO. It combines a high density (6.63 g/cm^3) with a high atomic number ($Z_{\text{eff}} \sim 54.4$), providing excellent photo-peak efficiency for the 342 keV emissions of ^{111}Ag. Its peak emission at 520 nm is optimally matched with the PDE of latest-generation SiPMs. Furthermore, the absence of intrinsic radioactivity, typical of Lutetium-based crystals, simplifies the background subtraction [16–18]. The short decay time can reduce signal dead time and pile-up events, thus these scintillators can be used for high count rate imaging [16, 19]. GAGG(Ce) can be manifactured in crystal arrays with ultra-small pixels, in which case the scintillator array demonstrates good overall spatial resolution, typically in the sub-millimeter FWHM range [20–22].

Within the ISOLPHARM-ADMIRAL (Advanced Dosimetry Methods and In Vitro Radiobiology of ^{111}Ag Labeled Radiopharmaceuticals) project, a dedicated gamma camera has been developed with a Hamamatsu SiPM 8 $\times$ 8 matrix, a GAGG(Ce) crystal matrix, a tungsten collimator and a readout by CAEN electronics. The aim of the experiment is to build a compact, cost-effective gamma camera suitable for ^{111}Ag imaging, for applications in laboratory or small animal tests. The design, electronic readout, and procedures for gain equalization and flood field testing are described in section 2, alongside the description of the simulation setup used to model the system. Experimental results and Monte Carlo validation, featuring measurements with a ^{133}Ba point-like source and ^{111}Ag extended sources, are presented in section 3.

2 Material

2.1 Device description

The integrated gamma camera system and its main components are illustrated in figure 1. It consists of a SiPM matrix, a matrix of GAGG(Ce) scintillators, an optical coupling with silicon pads, and a tungsten collimator. The technical specifications of the individual components are detailed below.

2026 JINST 21 P10036

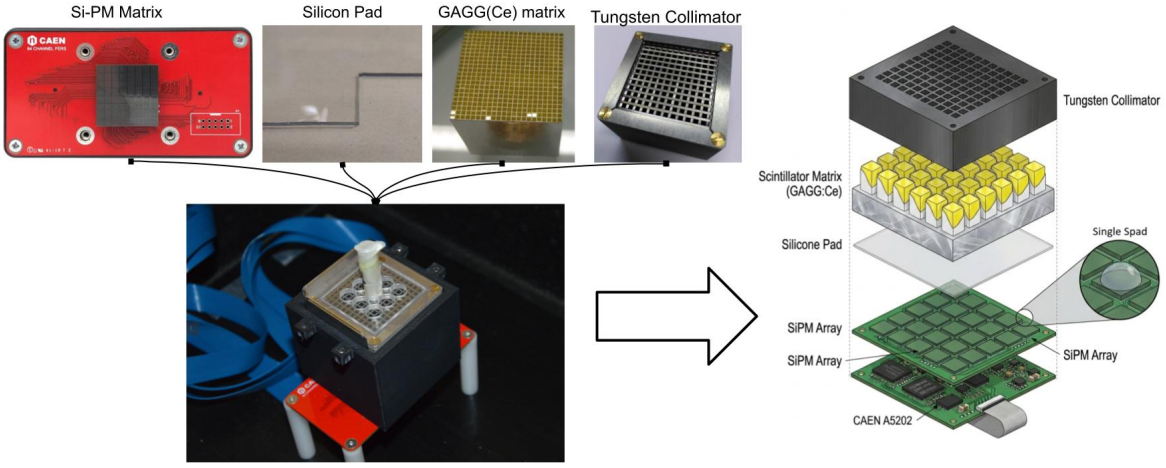


Figure 1. Hardware components and assembly of the gamma-camera prototype. (Top) Detailed photographs of the individual detector layers: the SiPM matrix mounted on the front-end PCB, the optical silicon pad, the GAGG(Ce) scintillator array, and the tungsten collimator. (Bottom left) The fully assembled detector module integrated within a light-tight enclosure for dark-count minimization and environmental light screening. The CAEN FERS readout electronics are interfaced via high-density cables (blue in the photo). (Right) Corresponding exploded-view schematic illustrating the vertical stack integration, including the CAEN A5202 readout board, the SiPM sensing layer with a detail of the single SPAD microcell, the scintillator matrix, and the collimator. Adapted with permission from [23]. Copyright © 2026 CAEN S.p.A. All rights reserved.

Photosensitive Array: a Hamamatsu S14160-3050HS-08 SiPM array [25] is employed as the detection plane. This device has 64 (8×8) channels, each one with photosensitive area of $3.0 \times 3.0\,\mathrm{mm}^2$ and geometrical fill factor of 74 %. The channels are separated by 0.2 mm of silicone resin so that the total dimension of the device is $25.8 \times 25.8 \times 1.35\,\mathrm{mm}^3$. The window refractive index is 1.57. The spectral response range is from 320 to 900 nm, with a peak sensitivity at 450 nm. The operating voltage was set to 42 V allowing for a correction of ±1.5 V for each pixel.

Scintillator Matrix: the detector utilizes a scintillator array composed of 23 × 23 GAGG(Ce) pixels, each with dimensions: $1 \times 1 \times 17\,\mathrm{mm}^3$, produced by Epic Crystal [26]. Each individual pixel is wrapped on four sides with a 0.2 mm thick $BaSO_4$ layer, which acts as a diffuse reflector. While the face coupled to the SiPM remains clear for light transmission, the remaining top face of each crystal and the entire external perimeter of the matrix are wrapped with a 0.03 mm thick aluminum foil. The resulting total dimensions of the assembled matrix are $27.86 \times 27.86 \times 17.23\,\mathrm{mm}^3$. GAGG-HL exhibits a density of $6.6\,\mathrm{g/cm}^3$, refractive index 1.91, and a light output of 54000 ph/MeV.

Collimator: the collimator used in this work was designed and manufactured by the mechanical workshop of INFN-Bologna. It was fabricated starting from a 1 mm thick tungsten foil. The foil was cut using a wire Electrical Discharge Machining (EDM) [27] to produce many copies of a comb-like unit. Later, the units were composed and inserted in a package to form a matrix with squared holes and septa of 1 mm thickness. The barrel of each hole has a side of 2 mm and a length of 30 mm. The collimator was placed in direct mechanical contact with the top surface of the GAGG(Ce) crystal, with no gap between the two components.

Optical coupling: the scintillator and the SiPM are optically coupled using a silicon pad of 2 mm thickness with refractive index 1.43 from Eljen Tecnology [28].

2026 JINST 21 P10036

Readout electronics: the SiPM array is interfaced with a CAEN A5202 [23] readout board through a dedicated A5251 adapter [29]. The A5202 board, based on two CITIROC 1A ASICs, performs the pre-amplification and digitization of the 64 independent channels. Board configuration, real-time pulse-height analysis, and data logging are managed using the CAEN-Janus software [30].

The experimental setup is illustrated in figure 2. The entire detection assembly was housed in a dark polystyrene box. This housing provides mechanical support and ambient light shielding, but offers no shielding against γ-ray radiation incident from outside the field of view of the camera. As a consequence, background measurements are required to characterize and subtract this contribution.

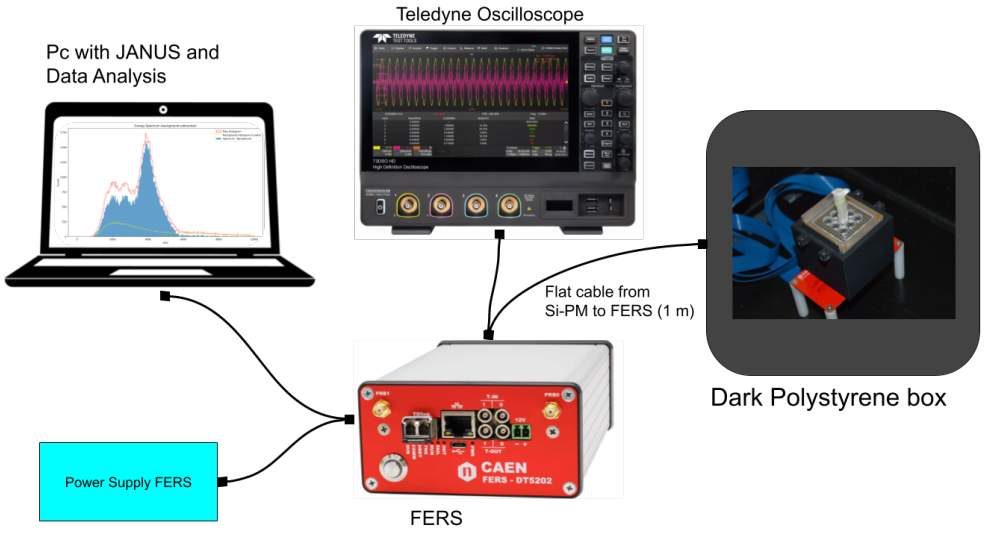


Figure 2. Experimental setup for the gamma camera characterization. The system includes the detector module housed in a light-tight polystyrene box, connected via a flat cable to the CAEN FERS-DT5202 readout unit. A Teledyne LeCroy oscilloscope is used for signal monitoring, while a dedicated workstation runs the Janus software suite for FPGA configuration, data acquisition (DAQ), and data analysis. Adapted with permission from [23]. Copyright © 2026 CAEN S.p.A. All rights reserved. Adapted with permission from [24].

It should be noted that, in this first prototype, no dedicated γ-ray shielding has been implemented. This is a design choice aimed at simplifying the mechanical assembly during the initial characterization phase. The integration of γ-ray shielding, together with an extension of the active area to increase the field of view, is foreseen in the next-generation detector.

2.2 Front-end electronics structure

The readout system is based on the CAEN A5202 board (FERS-5200 series), which integrates two Citiroc 1A ASICs produced by Weeroc [31, 32]. The board consists of a dedicated power supply module for SiPM biasing and an FPGA for logic management and data processing [33]. It provides 64 independent channels (32 channels per chip), each one directly connected to a single pixel of the SiPM array.

The Citiroc 1A architecture, derived from the EASIROC design [34], features an analog core that includes a preamplifier, followed by two separate chains for charge and time measurements [35–38]. The preamplifier offers two selectable gain stages — High Gain (HG) and Low Gain (LG) — with a gain ratio of approximately 10, to maximize the dynamic range [39]. The preamplifier of each

2026 JINST 21 P10036

channel can be individually disabled, allowing for the suppression of noisy pixels. Each of the two processing chains comprises an adjustable shaper, a track-and-hold circuit, and an active peak detector (PD). Furthermore, the gain of each SiPM pixel can be individually equalized by tuning its bias voltage via an integrated 8-bit digital-to-analog converter (DAC). This DAC provides a regulation range from 0 to 4.5 V relative to the common bias voltage, allowing for precise compensation of gain across the sensor array. The CAEN A5202 front-end unit incorporates an onboard digitally controlled high-voltage regulator (CAEN A7585D) connected to a temperature sensor on the adapter, that guarantees the stability of the system against thermal drifts.

Table 1. Main characteristics of the CITIROC chip [34].

Dimensions	16.5 mm^2 (4.1 × 4.1 mm)
Power Supply	4.5 V / 0 V
Inputs	32 voltage inputs with independent SiPM HV adjustments
Outputs	32 trigger outputs
	1 ASIC trigger output (Trigger OR) 1 multiplexed charge output
Integrated Configuration Mechanism	32 HV adjustments (8-bit) Trigger Threshold Adjustment (10-bit) Gain tuning (32 channels) Programmable Trigger Mask (for 32 Channels) 32 Channel Enable

The charge measurement is handled by a CR-RC^2 shaper. The shaping time can range from 12.5 ns to 87.5 ns with a 12.5 ns step. While this timing is globally set for all channels, it can be independently adjusted between the low-gain and high-gain sections of the ASIC [33]. For the measurements presented in this work, a shaping time of 87.5 ns was selected to match the scintillation properties of the GAGG(Ce) crystals.

The board can operate in four different modes: spectroscopy, counting, timing, and spectroscopy plus timing. In this study, the spectroscopy mode was employed. In this configuration, a global trigger, generated by the internal trigger logic, initiates the peak-sensing phase. This produces a data packet containing a common timestamp and the digitized energy values for each channel. The onboard Analog-to-Digital Converter (ADC) introduces a dead time of approximately 10 µs, allowing for a maximum trigger rate of 100 kcps.

The peak stretcher works in sequential phases: before the arrival of the trigger signal, peak sensing is disabled; when the trigger rises, the peak detector is activated and held until the programmed delay is reached, to capture the maximum amplitude of the input signal within a gate of 87.5 ns [33].

2.3 Pulse shape analysis

The analog chain of the CITIROC 1A ASIC was characterized by monitoring the preamplifier and shaper outputs through the A5202 front-end board probe pins. Figure 3 illustrates a representative event acquired during the calibration phase, obtained by illuminating the SiPM array with a NPL41B laser from THORSLAB (λ = [405] nm) [40]. The slow-shaper output (red trace in figure 3) exhibits a peaking time of approximately 300 ns, coming from the configured shaping time of 87.5 ns for a

2026 JINST 21 P10036

CR-RC^2. The pulse presents a bipolar profile with a controlled undershoot to facilitate rapid baseline restoration and mitigate pile-up effects during high-rate operation. For spectroscopy, only the peak amplitude of the positive component is processed by the peak-sensing ADC.

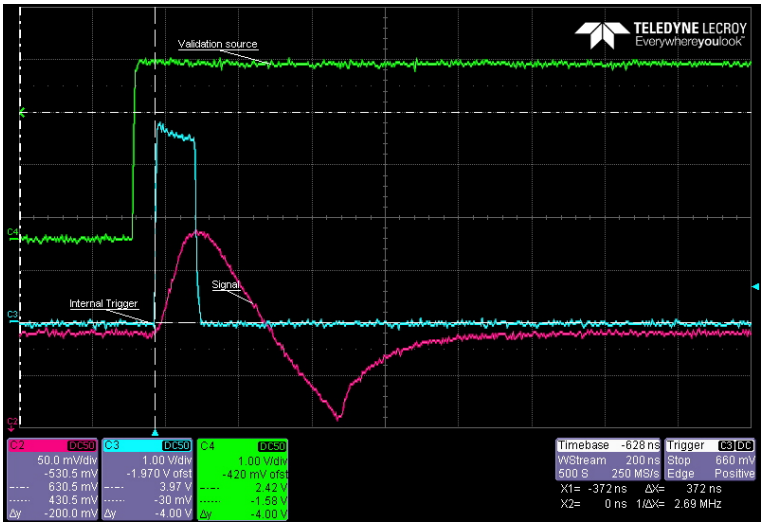


Figure 3. Oscilloscope traces showing the signal processing chain: the shaped pulse (C2 — red, 50 mV/div), the digital internal trigger (C3 — light blue, 1 V/div), and the validation logic signal (C4 — green, 1 V/div). Time scale is 200 ns/div.

The sampling of the pulse maximum is governed by a programmable delay between the initial trigger and the start of the hold phase (the "gate" within which the peak is captured). This delay was fixed at 250 ns, following the optimization study presented in ref. [33]. This value allows to sample signals at their maximum, accounting for the peaking time of the electronics and the scintillation decay constant of the GAGG(Ce) crystals.

2.4 Equalization of SiPM array

The response uniformity of a gamma camera is affected by two main factors: the breakdown voltage (bias) spread of the SiPM pixels and the non-uniformity of the readout preamplifiers. To compensate for both effects simultaneously, an integrated flat-field calibration was implemented. The experimental setup (Figure 4) consists of a pulsed laser source coupled to an optical fiber, mounted inside the A5251 CAEN adapter. To approximate a far-field flat-field illumination, a dedicated 25 cm light guide was 3D printed in two sections. A converging lens was integrated into the optical path to ensure uniform photon distribution over the bare SiPM surface. Neutral attenuator filters were employed to ensure that the SiPM signals remained within the linear dynamic range of the CITIROC-1A ADC.

Initially, the operating bias was set for each channel according to the breakdown voltage values provided by Hamamatsu. While these nominal settings provide a baseline for the SiPM operation, a preamplifier gain sweep was subsequently performed to further refine and equalize the response of the entire matrix. This sweep involved varying the ASIC preamplifier settings (Low Gain) from 5 to 45 DAC units. Below 5 DAC units, the signal amplitude was too low compared to the electronic noise, resulting in an insufficient Signal-to-Noise Ratio (SNR) to cross the hardware trigger threshold. Above 45 DAC units the amplified signals pushed the analog processing chain outside its linear dynamic range, leading to saturation of the ADC.

2026 JINST 21 P10036

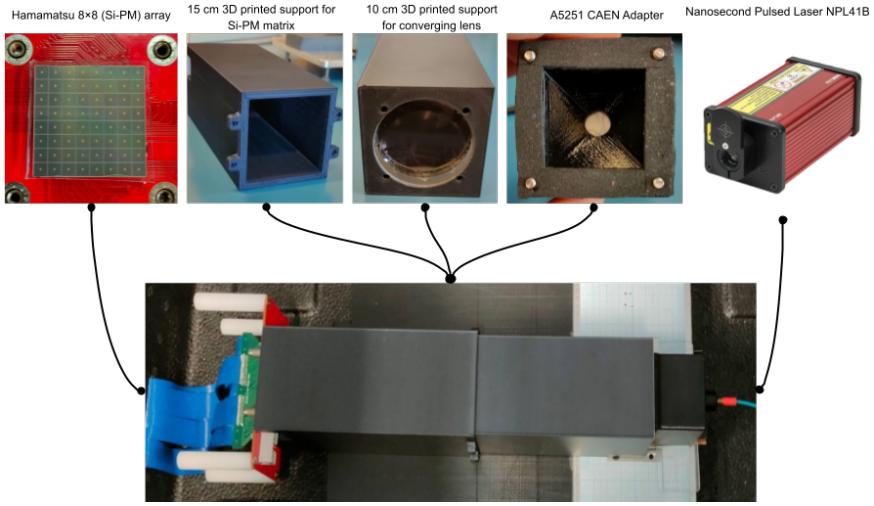


Figure 4. Exploded view (top) and assembled configuration (bottom) of the optical equalization setup. The system includes the SiPM array, a 3D-printed light guide (total length 25 cm), a converging lens for beam quasi-collimation, the CAEN A5251 mechanical adapter coupled to a pulsed laser from Thorslabs Inc. source via an optical fiber. Adapted with permission from [23]. Copyright © 2026 CAEN S.p.A. All rights reserved. Adapted with permission from [41]. Copyright © 1999–2026 Thorlabs, Inc.

Figure 5 illustrates the raw pulse height distributions in arbitrary Analog-to-Digital Units (ADU) for a representative subset of channels, before equalization. For each channel, the peak position of the distribution was extracted as a function of the preamplifier gain setting to construct individual response curves. A representative example of such curves, shown for all channels, is reported in figure 6. For the evaluated models (linear, quadratic, power-law and cubic), the power-law model provided the best agreement with the experimental data, with residuals for a representative channel (Ch. 46) remaining below 4 % across the full operating range.

Figures 7(a) shows the array response with only the manufacturer-recommended (Hamamatsu) bias voltage settings. A significant channel-to-channel spread (Diff = $(\mathrm{ADU}_{\mathrm{max}} - \mathrm{ADU}_{\mathrm{min}})/\mathrm{ADU}_{\mathrm{average}}$ = 10.8 %), arising from the combined effect of intrinsic SiPM response variability and preamplifier gain dispersion, is apparent.

The equalization procedure was initially verified via hardware by applying the individual preamplifier gain, coming from the power-law fit and a measurement was performed. The peak positions of the 64 channel distributions were extracted via Gaussian fit and the inter-channel spread was evaluated. Once the hardware-level correction was validated, it was converted into a set of multiplicative factors to be applied during post-processing. The per-channel multiplicative software correction factors were then calculated as:

$$f_i = \frac{\mathrm{ADU\text{-}peak}_{i,\,\mathrm{corrected}}}{\mathrm{ADU\text{-}peak}_{i,\,\mathrm{uncorrected}}} \tag{2.1}$$

where the corrected ADU peaks are those measured under the optimal hardware setting and the uncorrected ones refer to the baseline configuration. Applying these factors during post-processing replicates the hardware equalization without modifying the acquisition settings, ensuring consistency across all subsequent datasets.

2026 JINST 21 P10036

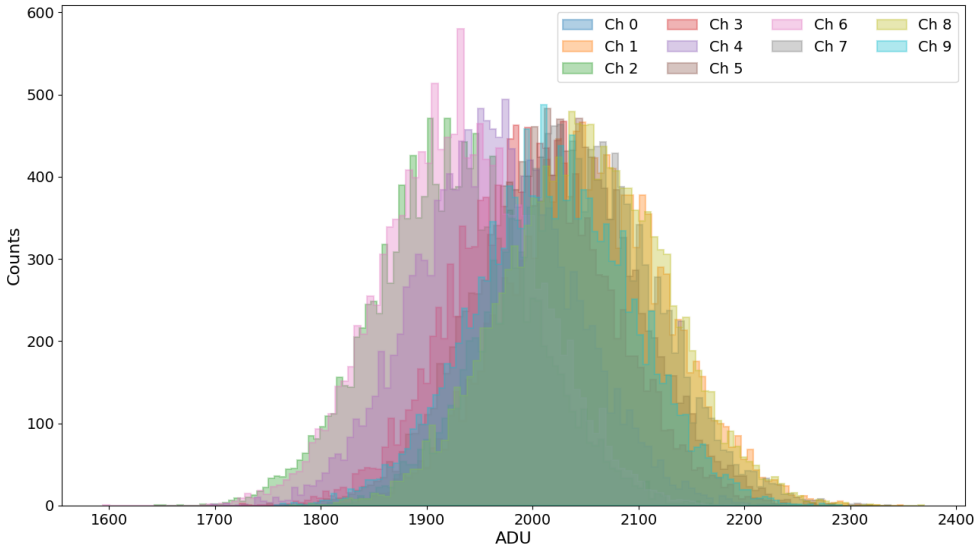


Figure 5. Pulse height distributions for a selection of ten SiPM channels at a fixed gain of 30 (arbitrary units). Each colored histogram corresponds to a different channel. The plot illustrates the raw SiPM response before the equalization procedure. The x-axis represents the integrated charge in Analog-to-Digital Units (ADU).

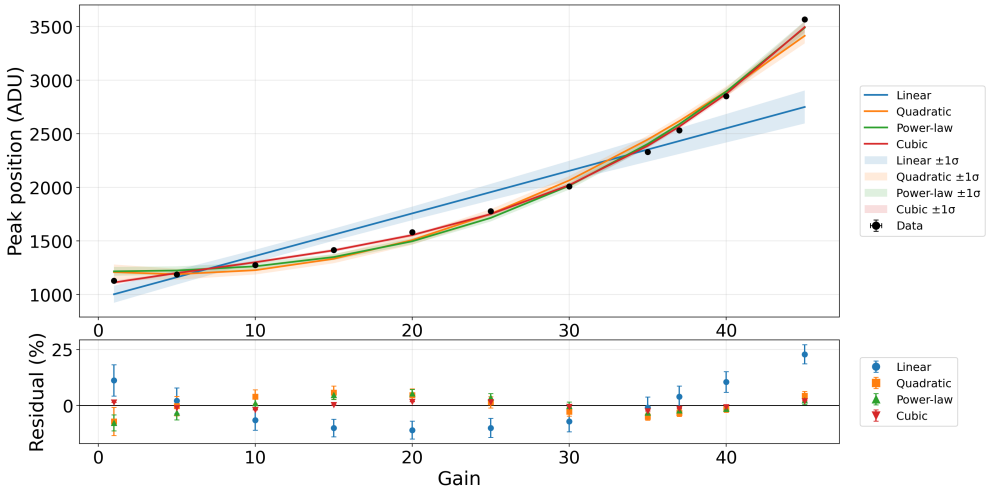
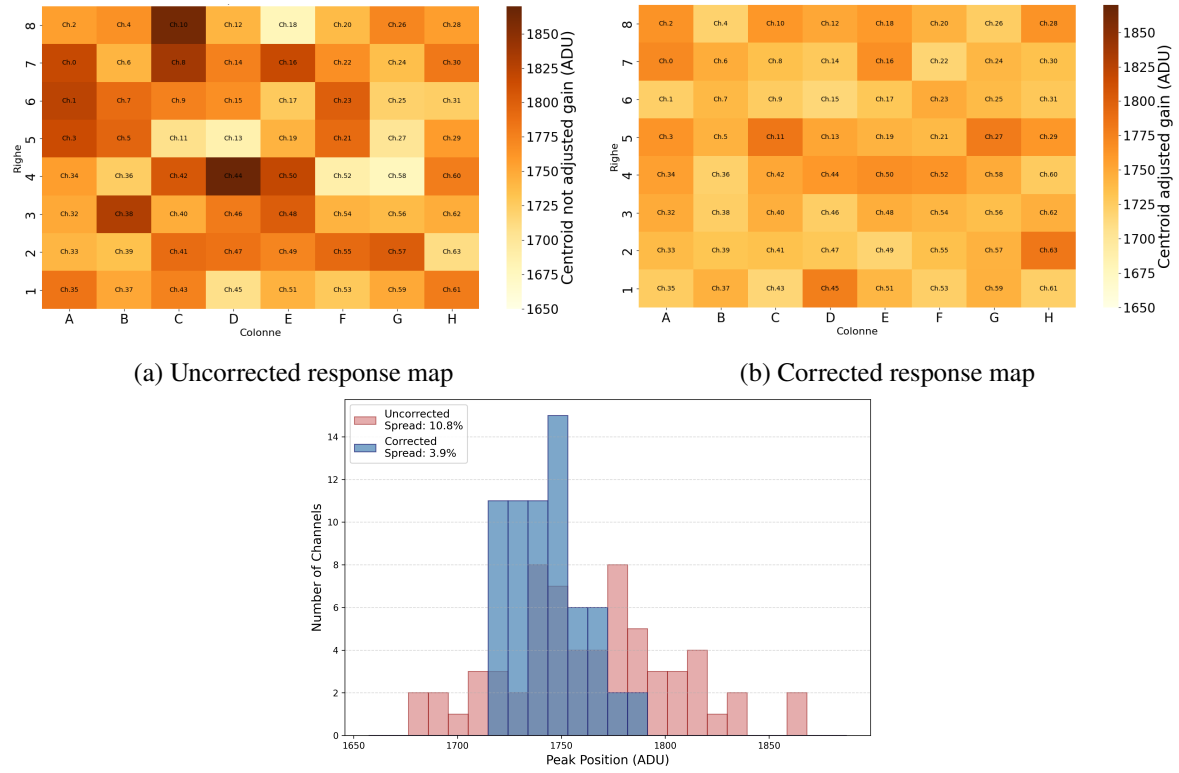


Figure 6. Gain calibration analysis for a representative SiPM channel (Ch. 46). The top panel shows the peak position (in ADU) as a function of the ASIC preamplifier gain, compared against four fitting models: linear, quadratic, power-law, and cubic. Shaded areas represent the $\pm 1\sigma$ confidence intervals for each fit. The bottom panel displays the percentage residuals for each model.

2026 JINST 21 P10036

After applying these coefficients, derived from a flat-field acquisition, the residual spread is reduced to Diff = 3.8 %, as shown in figure 7(b) and 7(c). This correction table is intrinsically linked to the specific SiPM matrix and its characteristic breakdown voltages.

The residual non-uniformity of 3.8 % represents the intrinsic precision limit of the equalization procedure. This dispersion is primarily attributed to statistical fluctuations during the flat-field acquisition and minor systematic uncertainties in the power-law modeling. Nevertheless, this residual spread is secondary compared to the mechanical tolerances in the scintillator-to-matrix alignment and the non-uniformities of the optical coupling layer, which dominate the overall system response as discussed below.



(a) Uncorrected response map

(b) Corrected response map

(c) Corrected response map

Figure 7. Raw response of the 64-channel SiPM array under uniform pulsed laser illumination. (a) 2D intensity map of the ADC peaks positions before the preamplifier gain equalization, showing significant channel-to-channel variations. The initial spread (10.8 %) is primarily attributed to intrinsic breakdown voltage variations among the SiPM pixels and the gain dispersion of the ASIC channels. (b) Equalized response of the detector array after the application of the fine-gain correction coefficients. The equalization procedure reduced the relative spread to 3.8 %. (c) 1D histograms of the ADU peak positions for all 64 channels before (red) and after (blue) the equalization procedure.

2.5 Monte Carlo simulations

A Monte Carlo application was developed to predict the performance of the gamma camera described above. This application is based on the well-known Geant4 toolkit, widely used to simulate the passage of particles in matter [43–45]. A first version has already been reported in a proceeding [46]. In

2026 JINST 21 P10036

Table 2. Geant4 simulation settings related to the implemented physics processes, including optical physics. The complete simulation, together with all details required for reproducibility, is available online [42]. Combining reflectivity (R) = 0 and transmittance (T) = 1 the photons propagates as if no interface is present. With R = 1, T = 0 and `dielectric_dielectric` type, the photons behaves according to the Snell's law of refraction. With R = 0.94, T = 0 and `dielectric_metal` type, there is a 6 % probability that the photon is absorbed while for the remaining 94 % it is reflected as if the interface is a mirror.

Physics list	`G4DecayPhysics`
	`G4RadioactiveDecayPhysics`
	`G4EmStandard Physics_option3`
	`G4OpticalPhysics`

GAGG(Ce) scintillator	scintillation yield 54000 photons/MeV, attenuation length 645 mm, refraction index 1.91
GAGG(Ce) rod skin surface	model `unified`, type `dielectric_metal`, finish `polished`, reflectivity 0.94, transmittance 0
GAGG(Ce) rod — optical coupling boundary	model `unified`, type `dielectric_dielectric`, finish `polished`, reflectivity 1, transmittance 0
optical coupling — SiPMs boundary	model `unified`, type `dielectric_dielectric`, reflectivity 0, transmittance 1

this section the main features will be summarized, focusing on the latest upgrades [42]. The settings employed in the Geant4 simulation are listed in table 2.

The collimator, scintillator array, optical coupling and SiPM array are constructed using the parameters indicated in section 2.1. In the simulations, either gamma-decaying radioactive nuclei or γ rays are generated. The γ rays which pass the collimator and release energy in the scintillator material generate optical photons. The optical photons which enter a SiPM are either recorded or discarded according to the Photon Detection Efficiency (PDE) declared in the SiPM array datasheet.

The behavior of the scintillation photons at the materials surfaces is defined by the configuration reported in table 2. The interface between each GAGG(Ce) rod and the surrounding reflector is modeled as a mirror so that the optical photons are reflected back. A more realistic diffuse-reflecting surface was tested but there was no noteworthy difference in the simulation outcome. Instead, the computational time increased several times; therefore, a polished reflector was modeled.

Absorption at the reflector optical surface induces a reduction of the number of optical photons that arrive at the SiPM array. Consequently, larger-absorbing surfaces determine worse energy resolution at the SiPM array. In literature, the reflectivity of $BaSO_4$ as a function of the photon wavelength is available [47]. Considering the wavelength range for the GAGG(Ce) optical photons (450–700 nm) the reflectivity value is about 97 %. Similarly, in the simulations the optical photons produced in this wavelength range undergo reflection at the $BaSO_4$ surface according to this value.

Crossing the boundary from the scintillator rod to the optical coupling, the optical photons are treated according to Snell's law of refraction. Instead, crossing the boundary from the optical coupling to the SiPM array, the optical photons continue on their trajectory regardless of the refraction indexes. This corresponds to an idealized treatment of the interface, effectively enforcing full transmission.

2026 JINST 21 P10036

This choice was adopted because a more realistic optical model led to a significantly lower light collection than what is observed experimentally.

To reproduce the energy resolution observed experimentally, an additional Gaussian smearing with 12.5 % standard deviation was applied to the simulated number of recorded optical photons. This term should be regarded as an effective description of the overall detector broadening. This broadening effect is probably caused by phenomena not included in the simulation framework, such as the read-out electronics. The Gaussian smearing was used to effectively account for these non-ideal effects. The order of magnitude of this parameter is supported by the experimental response of the observed non-uniformities (about 4 % under uniform laser illumination and about 5 % in the ^{111}Ag measurement), although slightly more conservative.

The output data contain: position and energy deposited by each γ ray interacting in the scintillator; number of optical photons detected by each SiPM in each event.

2.6 γ sources

Two radioactive sources were employed, each serving a different role in the detector characterization. A ^{133}Ba sealed γ ray source was employed. While the laser provided the response equalization of the matrix elements, the radioactive source was necessary for energy calibration checks, flood-field validation, and point-spread function (PSF) studies. Due to the presence of several emission lines in the energy region around the dominant 356 keV photopeak, ^{133}Ba provides a suitable benchmark for spectroscopic characterization. Measurements with ^{133}Ba were performed both in uncollimated geometry, with the source placed at a distance of 10 cm from the detector plane, and in collimated configuration for spatial-response studies.

An additional experimental campaign was carried out at the Laboratorio Energia Nucleare Applicata (LENA) in Pavia to characterize the gamma camera with ^{111}Ag, produced at the TRIGA reactor. ^{111}Ag has two main γ emissions at 342 keV (branching fraction: 6.7 %) and 245 keV (1.3 %). The absolute activity of the samples was verified with a calibrated HPGe detector, used as laboratory reference. The ^{111}Ag sources were prepared in aqueous solution and encapsulated in cylindrical plastic vials with diameters of 6 mm and 12 mm. At the time of acquisition, the activities of the three vials were 18.35 MBq, 7.37 MBq, and 7.39 MBq, respectively.

2.7 Data collection and analysis

The performance of the gamma camera prototype was evaluated through a sequence of laboratory measurements carried out under controlled and stable operating conditions. The datasets were collected with identical bias voltage and front-end gain settings, to ensure consistency throughout the characterization stages.

An event is acquired in correspondence with a trigger signal, that is generated when at least one channel exceeds a hardware programmed threshold. Although the full SiPM matrix (64 readout channels) is read out, only the 36 channels of the inner 6×6 region are enabled in the trigger logic and the edge channels are therefore acquired in slave mode. This configuration was adopted to reduce edge effects and light-collection non-uniformities at the crystal boundaries. For each event, the amplitude of the ADC signal in each channel is stored, together with the event timestamp.

For each event, the detector response was processed to extract two observables: the total detected signal amplitude, used as an estimator of the deposited energy, and the reconstructed interaction

2026 JINST 21 P10036

position in the detector plane. The total signal amplitude, $\mathrm{ADU_{tot}}$, was computed as

$$\mathrm{ADU_{tot}} = \sum_i \mathrm{ADU}_i, \tag{2.2}$$

where ADU_i denotes value measured on channel i. Depending on the applications, the sum can extend over all channels or over a 3×3 cluster, defined by a seed SiPM channel (the one with the largest signal amplitude) and its 8 neighboring channels.

Only channels with signal above a fixed threshold are considered, to reduce the impact of electronic noise. Prior to computing signal amplitude and reconstructed position, the ADU_i values were corrected for channel-to-channel non-uniformities using equalization factors derived from laser calibration data, as described in section 2.4. It should be acknowledged that this software equalization is applied in post-processing and does not affect the hardware trigger logic, which operates on the uncorrected signals. However, its impact on the final imaging performance is minor because the photopeaks of interest are well above the trigger threshold. The same threshold-filtered, gain-corrected signals were used for both signal amplitude and centroid reconstruction.

The amplitude and position signals obtained as described above are used for spectroscopic characterization, and spatial response measurements, as detailed in the following sections.

The interaction coordinates were reconstructed by means of a weighted centroid algorithm (Center of Gravity, CoG), defined as

$$x = \frac{\sum_i \mathrm{ADU}_i^n x_i}{\sum_i \mathrm{ADU}_i^n}, \qquad y = \frac{\sum_i \mathrm{ADU}_i^n y_i}{\sum_i \mathrm{ADU}_i^n}, \tag{2.3}$$

where ADU_i is the signal measured on channel i, (x_i, y_i) are the corresponding SiPM coordinates, and n is a parameter controlling the relative weight of the highest-amplitude channels [48]. In the present work, $n = 2$ was used.

Given the absence of γ-ray shielding in the detector enclosure (section 2.1), for each measurement, a dedicated background run was acquired under identical operating conditions but without the radioactive source. Background contributions were then subtracted from the source spectra and spatial distributions by scaling the background run to the same acquisition time as the source measurement.

The experimental campaign was organized in three steps, summarized in figure 8. First, a flood-field measurement was performed to verify the correct operation of the detector and the capability of the readout chain to resolve the individual scintillator pixels. Second, uncollimated spectroscopic measurements were performed to validate the energy calibration and quantify the intrinsic energy response of the GAGG(Ce)-SiPM assembly. Finally, collimated acquisitions were used to evaluate the spatial response of the system, including PSF studies, source-size reconstruction, and multi-source discrimination.

In the spectroscopic analysis, the photopeak position and width were extracted by fitting a Gaussian function to the background-subtracted spectrum within a narrow Region of Interest (ROI) centred on the photopeak. Since the background run was subtracted prior to fitting, no additional analytical background component was included in the fit; the ROI selection further ensures that residual Compton continuum contributions outside the photopeak region are excluded. The energy resolution was quantified as the ratio between the Full Width at Half Maximum of the Gaussian and the peak centroid position (FWHM/E).

2026 JINST 21 P10036

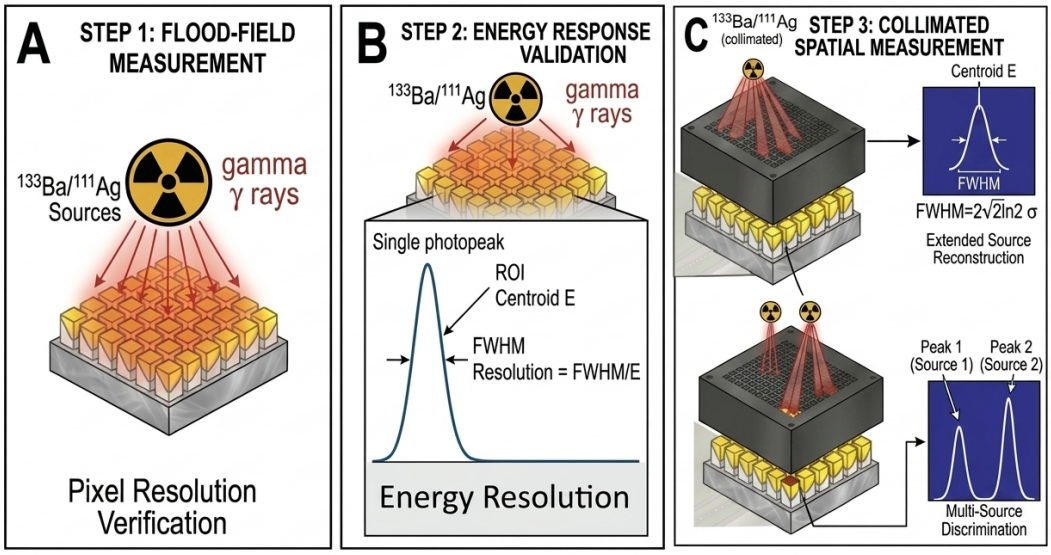


Figure 8. Experimental characterization workflow for the GAGG(Ce) scintillator array with SiPM readout, divided into three steps. (A) Flood-Field Measurement. A ^{133}Ba/^{111}Ag source uniformly irradiates the detector stack to verify individual channel operation and the 3×3 scintillator pixel grid. (B) Energy Resolution. Uncollimated spectroscopic measurements are used to extract the intrinsic energy resolution (FWHM/E) from a single-photopeak Gaussian fit. (C) Collimated Spatial Measurement. A collimated ^{133}Ba/^{111}Ag source evaluates: the Point Spread Function (PSF) and source localization via a localized Center-of-Gravity (CoG) pixel grid; extended source reconstruction via 2D Gaussian fitting (FWHM); and dual-source discrimination capability.

Prior to the CoG image reconstruction,events were gated within a $\pm 2\sigma$ energy window around the respective photopeaks. This statistical threshold retains between 52 % and 61 % of the total triggered events for both experimental and simulated data. The full spectrum (over 96 % of triggered events, after excluding a high-energy tail associated with muons and saturated/pile-up events) nominally increases the statistics but it includes degradation in the spatial reconstruction, introducing asymmetric blurring and shifting the reconstructed centroids in multi-source geometries. The two-dimensional distributions, reconstructed with the CoG analysis, were fitted with Gaussian models, and the spatial widths were reported in terms of full width at half maximum (FWHM).

In the following sections, these spatial distributions are referred to as "reconstructed images".

3 Results

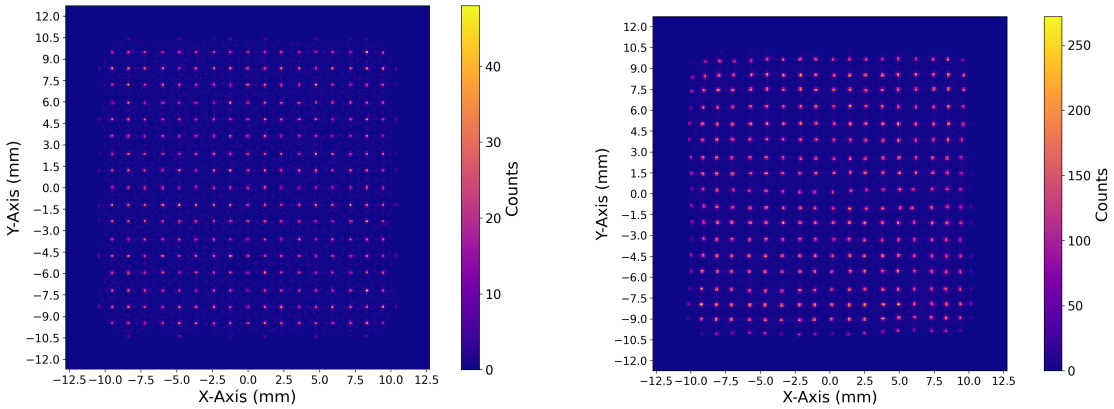
The calibration and benchmarking strategy was based on two complementary references: ^{133}Ba for flood-field validation, and point-like response characterization; ^{111}Ag for application-oriented spectroscopy and imaging tests with extended source geometries.

3.1 Flood field with ^{133}Ba

A flood-field irradiation was first performed using the ^{133}Ba source in order to verify the proper operation of the detector and the capability of the system to resolve the individual scintillator pixels. A two-dimensional histogram of reconstructed interaction positions was generated, as shown in figure 9. For this visualization, the weighted CoG implementation described above was adopted, as it provided

2026 JINST 21 P10036

a slightly cleaner separation of adjacent scintillator elements, although no significant change was observed in the main reconstructed quantities. The flood image provides a qualitative assessment of the light-sharing scheme, optical coupling, and position reconstruction, allowing a direct visualization of the separation between adjacent crystal elements. The result demonstrates that all crystal elements are clearly resolved and correctly mapped. As expected, because the hardware trigger is restricted to the inner 6×6 SiPM region (as detailed in section 2.7), the reconstructed image resolves the central grid of approximately 17×17 scintillator pixels rather than the full 23×23 physical array. At this stage, no quantitative flood-field figure of merit was extracted yet, as the purpose of the measurement was limited to a characterization of the detector response and channel equalization [49].



(a) Simulated 2D image pixels

(b) Experimental 2D image

Figure 9. Acquisition of ^{133}Ba placed on top of the GAGG(Ce), at 10 cm without the collimator in the central position. Left is the simulation and right is the experiment. The experimental image was acquired for a total time $\Delta t = 347$ s, collecting a total of 322243 events. No energy gating was applied to the events shown in this plot.

3.2 Spectroscopic response

3.2.1 ^{133}Ba energy spectrum

An uncollimated ^{133}Ba measurement was used to validate the intrinsic energy response of the prototype in its current configuration. The corresponding spectrum is shown in figure 10. Due to the intrinsic resolution of the GAGG(Ce) crystals and the present electronic noise level, the individual gamma lines at 276, 302, 356, and 383 keV are not fully resolved and appear as a blended peak dominated by the 356 keV emission.

The quantitative comparison between data and Monte Carlo simulation is summarized in table 3. The measured energy resolution at 356 keV is 29 ± 1 %, to be compared with 26 ± 1 % in simulation. The broader response observed in the experimental data ($\Delta E = 3$ %) can be attributed to contributions from electronic noise, which are not included in the idealized detector model, the presence of background in experimental data which is not included in the simulation, and local non-uniformities in light collection at the scintillator-SiPM interface. The simulation accurately reproduces the double-structure of the spectrum, consisting of the main blended photopeak dominated by the 356 keV emission and a lower-energy structure below 200 keV, primarily associated with Compton scattering. The slight residual excess in the experimental low-energy continuum can be attributed to environmental back-

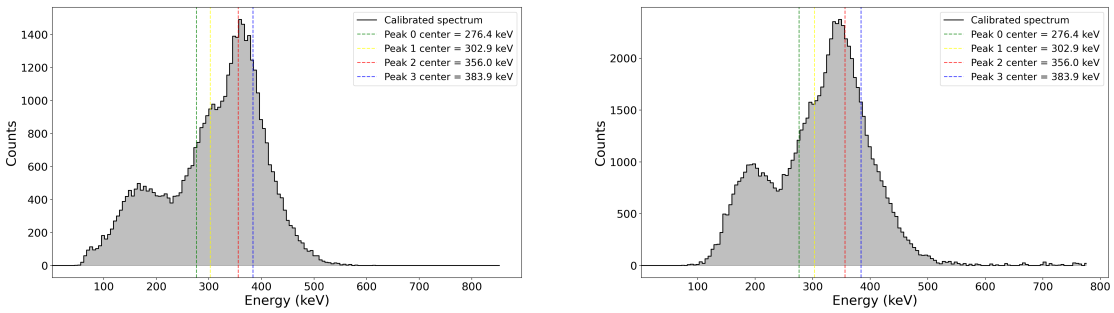
2026 JINST 21 P10036

scattering (such as the unshielded enclosure), as well as fluctuations of the discriminator thresholds of the front-end ASICs, which are not fully mapped in the idealized Monte Carlo model.

Table 3. Comparison of experimental and simulated spectroscopic parameters for ^{133}Ba.

	Energy Resolution (% @356 keV)	**Peak (ADU)**	**FWHM (ADU)**
^{133}Ba Data	29 ± 1	4377 ± 28	1290 ± 62
Simulated	26 ± 1	4356 ± 19	1120 ± 26

The fit model, used to extract the photopeak position and FWHM, consists of four Gaussian components corresponding to the main ^{133}Ba emission lines at 276.4, 302.9, 356.0, and 383.9 keV, plus an empirical Compton continuum. The relative amplitudes of the four Gaussian components were constrained to their known emission intensities [50], while their centroid positions were linked through a linear energy-ADU relation anchored to the dominant 356.0 keV line. The four fitted centroids in ADU were then used to derive a linear calibration function. This multi-component fit was employed exclusively to establish an accurate, physically constrained ADU-to-keV calibration for the blended spectrum. It was not used to define the energy window for image reconstruction, which instead relied on the simple numerical thresholds detailed in section 2.7 The simulated and measured spectra shown in figure 10(a) and figure 10(b) are directly displayed in energy units.



(a) Simulated total charge (calibrated)

(b) Experimental total charge (calibrated)

Figure 10. Energy-calibrated γ-ray energy spectra of the ^{133}Ba sealed source. The left panel shows the simulation and the right panel the experimental result. The ADU-to-keV calibration was derived from a weighted linear fit to the four peak centroids extracted from the spectral fit. The dashed vertical lines indicate the ^{133}Ba emission energies at 276.4, 302.9, 356.0, and 383.9 keV, used as calibration points. Background subtraction was applied only to the experimental data.

3.2.2 ^{111}Ag energy spectrum

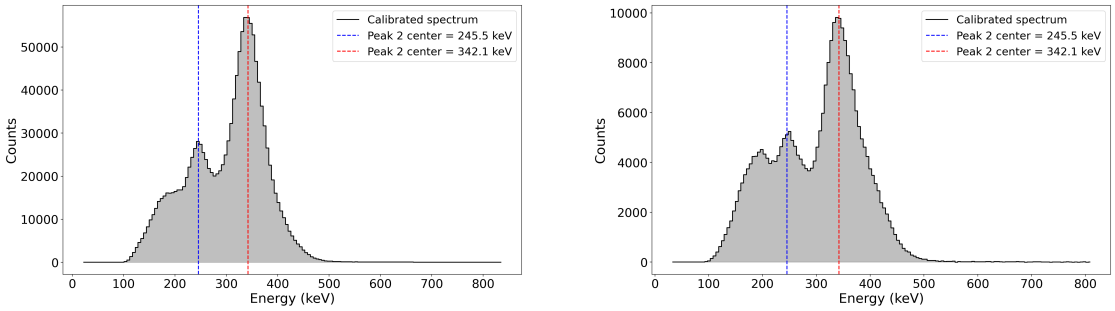
The spectroscopic response was also studied with the ^{111}Ag sources. The measured spectrum is dominated by the 342 keV photopeak and is shown, together with the Monte Carlo prediction, in figure 11(a) and figure 11(b), directly displayed in energy units. The ADU-to-keV calibration was derived independently using the two ^{111}Ag emission lines at 245.5 and 342.1 keV, following the same linear procedure applied to the ^{133}Ba data. The resulting calibration coefficients are consistent with those obtained from the barium source ($k_{\mathrm{Ag}} = 0.078 \pm 0.002$ keV/ADU, $k_{\mathrm{Ba}} = 0.078 \pm 0.006$ keV/ADU), confirming the linearity of the detector.

2026 JINST 21 P10036

The corresponding fit results are reported in table 4. In this case, the agreement between measurement and simulation is improved with respect to the ^{133}Ba study: the measured energy resolution is 23.1 ± 0.6 % at 342 keV, compared with 21.8 ± 0.3 % in simulation.

Table 4. Comparison of experimental and simulated spectroscopic parameters for ^{111}Ag

Dataset	**Energy Resolution (% @342 keV)**	**Peak Position (ADU)**	**FWHM (ADU)**
^{111}Ag Data	23.1 ± 0.6	3936 ± 7	910 ± 25
Simulated	21.8 ± 0.3	3915 ± 3	855 ± 13



(a) Simulated total charge (calibrated)

(b) Experimental total charge (calibrated)

Figure 11. Calibrated energy spectra of ^{111}Ag measured with the large vial placed above the GAGG(Ce) detector without collimator. The left panel shows the simulation and the right panel the experimental result. The linear ADU-to-keV calibration was derived from a weighted linear fit to the two peak centroids extracted from the spectral fit. The dashed vertical lines mark the fitted centroid positions. The dashed vertical lines indicate the ^{111}Ag emission energies at 245.5 and 342.1 used as calibration reference points. Background subtraction was applied only to the experimental data.

3.3 System efficiency

The efficiency of the gamma camera was measured using the setup with one small vial placed on the collimator (Figure 13), using the full γ spectrum, namely Compton and full-energy peaks of the 245 keV and 342 keV lines (total branching ratio ~ 8.0 %). The formula that relates the number of detected events to the number of ^{111}Ag decays is:

$$N_{\text{det,tot}} = A_{111\text{Ag}} \cdot (\Gamma_{342\text{keV}} + \Gamma_{245\text{keV}}) \cdot \Delta t \cdot \epsilon, \tag{3.1}$$

where $N_{\text{det,tot}}$ is total number of observed events, $A_{111\text{Ag}}$ is the ^{111}Ag activity, Γ are the branching ratios of the ^{111}Ag decay to the two γ emissions, Δt is the measurement time, and ϵ is the gamma camera efficiency. Since the measurement time is much smaller than the ^{111}Ag half-life, $A_{111\text{Ag}}$ is considered constant.

Using the measured counting rate, an experimental efficiency of approximately $\epsilon_{\text{exp}} \sim (2.1 \pm 0.1) \times 10^{-4}$ is obtained that lies within the range typically observed for parallel-hole collimator systems [5]. This result was directly compared with the Geant4 Monte Carlo simulation performed under identical experimental conditions, which predicted an expected detection efficiency of $\epsilon_{\text{sim}} = (2.5 \pm 0.1) \times 10^{-4}$.

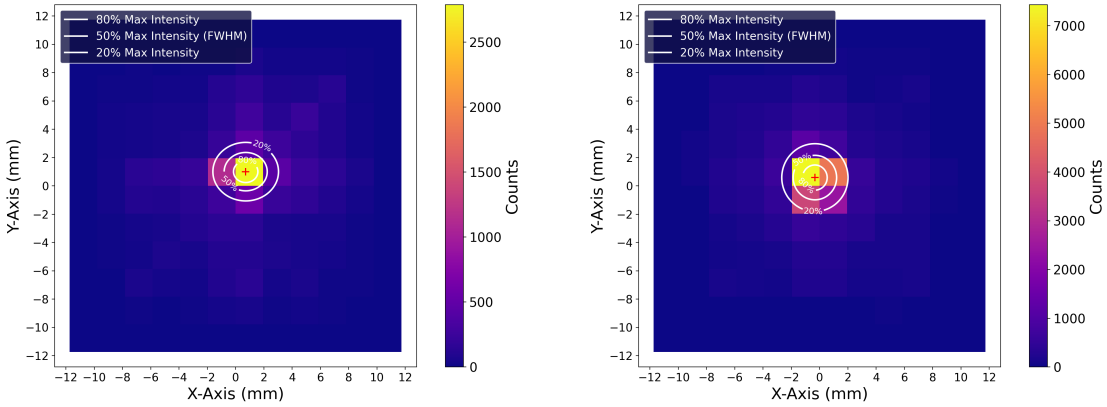
2026 JINST 21 P10036

This value is larger than the experimental estimate by about 15–18 %, the discrepancy can be attributed mainly to the incomplete description of light collection and the simplified treatment of the electronic response.

3.4 Spatial response and imaging performance

3.4.1 ^{133}Ba point-source response

The system spatial response, PSF, of the gamma camera was evaluated with a collimated ^{133}Ba source used as a point-like source. The source was positioned directly above the collimator aperture in order to approach quasi-point irradiation conditions. The reconstructed 2D images for both data and Monte Carlo simulation are shown in figure 12. In both cases, the response exhibits a Gaussian-like profile, consistent with a point-source response.



(a) Simulated 2D image

(b) Experimental 2D image

Figure 12. Reconstructed 2D response of the gamma camera to a point-like ^{133}Ba sealed source: Monte Carlo simulation (left) and experimental measurement (right). The color scale represents the event density. The red cross marks the reconstructed centroid, while the white contours indicate the 20 %, 50 % (the FWHM), and 80 % maximum intensity thresholds used to characterize the PSF in compliance with NEMA standards. The experimental image was acquired for a total time $\Delta t = 2764$ s, collecting a total of 72134 events. Events were gated within a $\pm 2\sigma$ energy window to select the main photopeak region and reject Compton scattering.

The spatial resolution was quantified by fitting the distributions with a two-dimensional Gaussian model. The results are summarized in table 5. The measured FWHM values, 3.0 ± 0.6 mm and 3.0 ± 0.5 mm along the two axes, are in agreement with the expectations from the simulation. This agreement supports the consistency of the optical transport and noise parametrization implemented in the Monte Carlo model.

Table 5. Spatial reconstruction parameters for the ^{133}Ba point source at 356 keV. Values are expressed as Mean ± Standard Deviation from the 2D Gaussian fit.

Dataset	**FWHM$_x$ (mm)**	**FWHM$_y$ (mm)**
^{133}Ba Data	3.0 ± 0.1	3.1 ± 0.1
Simulated	3.0 ± 0.2	3.0 ± 0.1

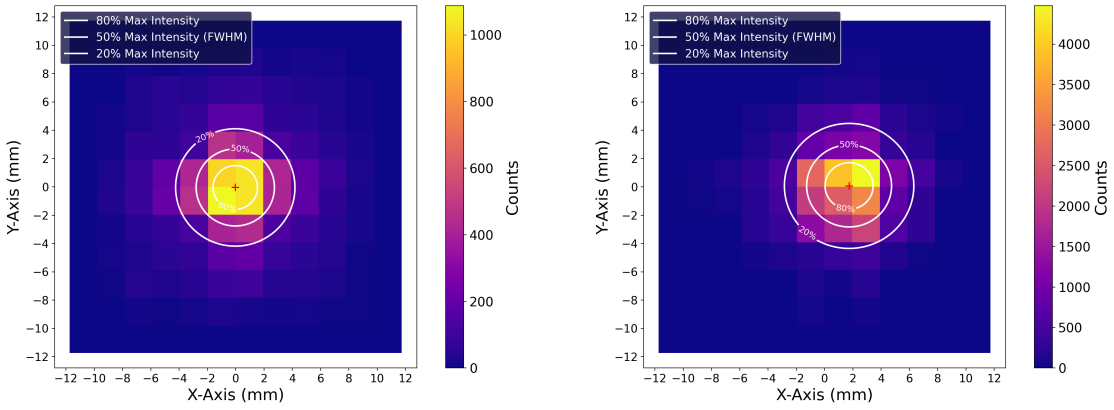
2026 JINST 21 P10036

It was observed that the reconstructed shape is sensitive to the source alignment relative to the collimator geometry. In particular, the interaction between the nominal source position and the square collimator holes may introduce small asymmetries in the PSF. This sampling effect is most visible for nearly point-like sources and is expected to be less pronounced for extended activity distributions. For distances greater than 30 mm, the spatial resolution degrades linearly due to the projective geometric effect of the parallel-hole collimator. According to the simulation, the system exhibits a FWHM = 5.0 ± 0.2 mm at 3 cm, and a FWHM = 8.6 ± 0.1 mm at 5 cm.

3.4.2 ^{111}Ag collimated imaging with a 6 mm vial

The imaging capability for an extended source was then evaluated using a 6 mm diameter vial filled with ^{111}Ag and positioned directly on top of the collimator. While the source was placed exactly in the center of the detector system in the Monte Carlo simulation, the relative positions could not be precisely controlled in the laboratory. For these measurements, event-by-event reconstruction was performed with the localized CoG algorithm.

The resulting images, with pixel positions converted to millimeters, are shown in figure 13. As expected given the square geometry of the collimator holes and the discrete SiPM lattice, the reconstructed distributions reflect this underlying pixelated structure. No interpolation or smoothing filters (such as Gaussian filtering) were applied to the data in order to preserve and display the raw spatial sampling performance of the prototype.



(a) Simulated 2D image

(b) Experimental 2D image

Figure 13. Acquisition of the 6 mm vial containing ^{111}Ag placed at the center of the collimator. The left panel shows the simulation and the right panel the experimental result. The red cross marks the reconstructed centroid, while the white contours indicate the 20 %, 50 %, and 80 % maximum intensity thresholds. The experimental image was acquired for a total time Δt = 798 s, collecting a total of 105125 events. Events were gated within a $\pm 2\sigma$ energy window to select the main photopeak region and reject Compton scattering.

The results of the 2D Gaussian fit are summarized in table 6. The measured FWHM, approximately 6.0 mm along both coordinates, is in good agreement with the Monte Carlo expectation for the same source, demonstrating the high fidelity of the gamma camera and the accuracy of the system spatial response.

2026 JINST 21 P10036

Table 6. Centroid coordinates and spatial resolution (FWHM) for the 6 mm ^{111}Ag vial.

Dataset	Center X(mm)	Center Y(mm)	FWHM$_x$ (mm)	FWHM$_y$ (mm)
^{111}Ag Data	1.74 ± 0.07	−0.06 ± 0.07	5.9 ± 0.2	5.9 ± 0.2
Simulated	0.01 ± 0.05	−0.03 ± 0.05	5.6 ± 0.1	5.6 ± 0.1

The small broadening observed in the experimental data with respect to simulation is consistent with residual optical light spreading and electronic effects contributions not fully accounted for in the idealized detector model.

To evaluate the optimal trade-off between imaging efficiency and spatial resolution, an alternative asymmetric gating window (with a lower limit extended down to approximately 215 keV) was also tested to explicitly include the 245 keV secondary emission of ^{111}Ag. For the single source, this wider window increased the fraction of retained useful events for imaging from 52.4 ± 0.2 % to 70.2 ± 0.1 % in the experimental data, and from 61.3 ± 0.3 % to 77.8 ± 0.3 % in the Monte Carlo simulation. However, the experimental FWHM changed from 5.9 ± 0.2 × 5.9 ± 0.2 mm to 6.3 ± 0.2 × 6.2 ± 0.2 mm. Although these spatial profiles remain compatible within statistical uncertainties, the $\pm 2\sigma$ symmetric window around the main 342 keV photopeak was maintained as reference methodology for this prototype, to minimize the inclusion of low-energy scatter from the collimator.

3.4.3 Spatial linearity and multi-source reconstruction

A further imaging test was performed to assess the capability of the prototype to resolve two nearby radioactive sources and to reconstruct their relative distance. Two identical 6 mm diameter vials filled with ^{111}Ag, with activities of 7.34 MBq and 7.56 MBq, respectively, were placed on the collimator using a plastic holder with a nominal center-to-center distance of 9 mm.

The reconstructed images are shown in figure 14. The two activity distributions are clearly separated in both the measurement and the simulation. The CoG algorithm, combined with the photopeak energy gating described in the previous section, allows a clean separation of the two intensity distributions.

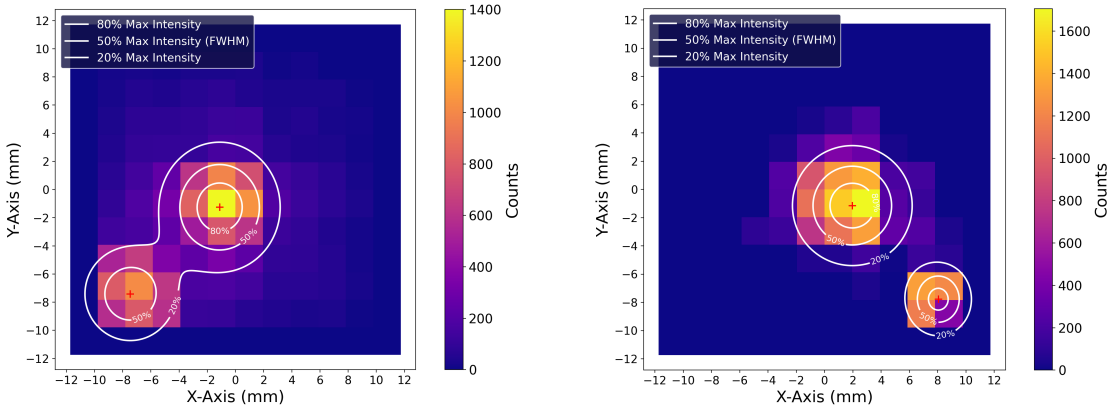
The centroids of the two sources were determined by performing a double 2D Gaussian fit on the experimental and simulated data. The reconstructed source separation is reported in table 7. The experimental value, 9.00 ± 0.35 mm, is in agreement with the nominal distance imposed by the holder.

Table 7. Distance between the reconstructed centroids of two vials obtained from experimental data (LENA) and Monte Carlo simulation. The uncertainty is derived from standard Gaussian error propagation on each coordinate.

Dataset	Distance between vials (mm)
^{111}Ag Data	9.7 ± 0.7
Simulated	9.4 ± 0.5

It was checked that when applying an extended gating window (down to ~ 215 keV) to the dual-source setup, the experimental imaging efficiency increased from 52.6 ± 0.1 % to 69.8 ± 0.1 %, but the reconstructed center-to-center distance shifted to 10.07 ± 0.17 mm. This significant overestimation of the nominal 9.0 mm separation confirms that the inclusion of low-energy scatter and cross-talk perturbs the Center of Gravity calculation, making the strict $\pm 2\sigma$ photopeak gate suggested to preserve

2026 JINST 21 P10036



(a) Simulated 2D image

(b) Experimental 2D image

Figure 14. Simultaneous acquisition of two 6 mm ^{111}Ag vials placed at a nominal distance of 9 mm. The left panel shows the Monte Carlo result and the right panel the corresponding experimental measurement. The experimental image was acquired for a total time $\Delta t = 893$ s, collecting a total of 158401 events. Events were gated within a $\pm 2\sigma$ energy window to select the main photopeak region and reject Compton scattering.

spatial positioning accuracy in multi-source environments. A systematic study of this effect is planned after the acquisition of additional dual-source ^{111}Ag data and will be reported in a future work

3.5 Preliminary phantom imaging

As a proof-of-concept for potential biomedical applications, a preliminary test was carried out with a commercial mouse phantom by Bioemtech [51]. The phantom is a 3D-printed realization based on the Digimouse whole-body mouse atlas [52], and contains several compartments corresponding to distinct organs, each of which can be filled independently with radioactive solution. In the present study, the bladder, kidneys, and liver compartments were filled with ^{111}Ag for a total activity of 15.7 MBq. A qualitative reconstruction of the resulting activity distribution is shown in figure 15.

The CoG reconstruction allows the visual localization of the active regions, demonstrating that the current hardware is capable of capturing spatially structured activity distributions.

However, a quantitative segmentation of the individual compartments is still limited by the absence of γ-ray shielding in the detector enclosure (section 2.1), which allows uncollimated photons from out-of-field compartments to produce a diffuse background contribution, the overlap of the scintillation light distributions, and the finite sampling of the detector system. For this reason, the phantom measurement should be regarded as a preliminary validation rather than as an imaging study.

Future work will focus on improving the reconstruction of complex activity distributions by adopting more advanced position-estimation techniques, such as mean square estimation (MSE)-based methods [53] or super-resolution reconstruction (SRR) approaches [54]. These developments are expected to improve organ separation.

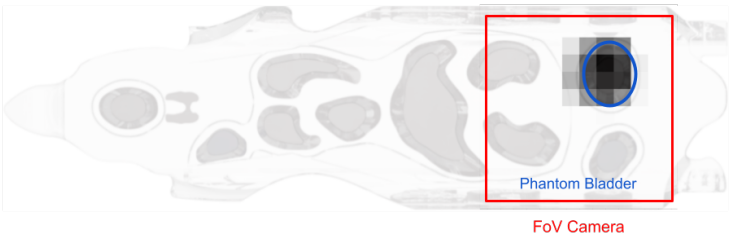
3.6 Spatial linearity and resolution accuracy

The spatial resolution of approximately 3 mm FWHM measured with the present parallel-hole tungsten collimator is consistent with the expected performance for this geometry. In parallel-hole collimators the system resolution is determined by the quadratic combination of the intrinsic detector resolution and

2026 JINST 21 P10036



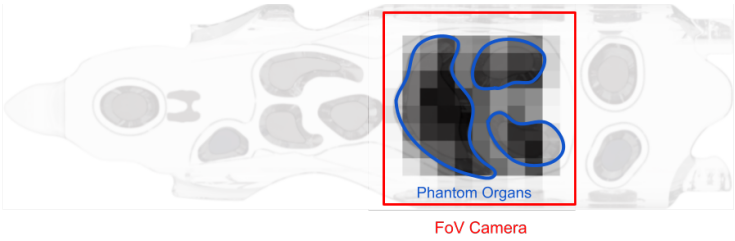
(a) Photo of the Bioemtech phantom [51].



(b) Image of the Phantom over-imposed to the reconstructed images, with ^{111}Ag in one bladder.



(c) Image of the Phantom over-imposed to the reconstructed images, with ^{111}Ag in one bladder and 2 kidneys.



(d) Image of the Phantom over-imposed to the reconstructed image, with ^{111}Ag in the 2 kidneys and the liver.

Figure 15. Imaging of a 3D-printed mouse phantom by Bioemtech. (a) Photo of the mouse phantom during the ^{111}Ag activity measurement with the germanium detector. (b) Reconstructed γ ray images (gray color scale) overlaid on the phantom geometry showing the uptake in the bladder, with an activity of 2.3 MBq. The red square shows the Field of View (FoV), while the blue contours delineate the actual anatomical boundaries of the organs within the phantom, for spatial reference. The image was acquired for a total time Δt = 1224s, collecting a total of 79117 events. (c) Reconstructed γ ray image overlaid on the phantom geometry showing the uptake in the bladder and 2 kidneys, with an activity of 7.7 MBq. The image was acquired for a total time Δt = 1250 s, collecting a total of 153664 events. (d) Reconstructed γ ray image overlaid on the phantom geometry showing the uptake in the liver, kidneys, and bladder, with an activity of 15.7 MBq. The image was acquired for a total time Δt = 1204 s, collecting a total of 272733 events. Events were gated within a $\pm 2\sigma$ energy window to select the main photopeak region and reject Compton scattering. Adapted with permission from [51]. © 2026 Bioemtech. All rights reserved.

2026 JINST 21 P10036

the geometric collimator resolution, which depends on hole diameter, length, and source distance [5]. Sub-millimeter intrinsic spatial resolution has been reported for finely pixelated GAGG(Ce) arrays coupled to SiPM readout [20]. In this geometry, the spatial resolution is dominated by the parallel-hole collimator. The continuous position estimation provided by the CoG algorithm blurs the underlying discrete GAGG pixelation. The mismatch between the crystal pitch (1 mm) and SiPM channel pitch (3.2 mm) acts as an additional broadening factor. In detectors based on pixelated scintillator arrays coupled to SiPM readout, the detector architecture is typically optimized for spatial localization rather than for high-resolution gamma spectroscopy. In such configurations the energy resolution is influenced by light sharing between adjacent pixels and by the summation of signals from multiple readout channels during position reconstruction [55].

3.7 Discussion

Taken together, the experimental results indicate that the ISOLPHARM-ADMIRAL gamma camera prototype provides a stable and internally consistent response in both spectroscopic and imaging configurations. The agreement observed between experimental data and Monte Carlo simulations confirms that the detector model captures the main features of the system response. Remaining discrepancies can be attributed to non-ideal optical coupling, electronic effects, and mechanical tolerances that are not fully included in the simulation.

One limitation emerging from the present studies is related to the sampling uniformity. The collimator, scintillator, and SiPM array have different characteristic pitches, namely 3 mm, 1.2 mm, and 3.2 mm, respectively. As a consequence, the reconstructed response depends on the source position within the xy plane, and both efficiency and spatial resolution become position dependent [5]. Pushing the performance beyond the ones reported in this work would require an optimization of the collimator geometry and positioning, also in relation with the underlying scintillator array. The discrepancies observed between ideal simulated efficiencies and experimental spatial fidelity when including lower-energy emissions highlight the impact of unmodeled room scatter and environmental background. Future developments will involve dedicated background shielding and higher-statistics acquisitions to fully assess whether low-energy secondary emissions can be effectively recovered without compromising spatial fidelity. Furthermore, the observation that low-energy scattered events should be excluded from image reconstruction to preserve spatial fidelity suggests that future iterations of the prototype could benefit from higher hardware trigger thresholds. Real-time rejection of the Compton continuum would significantly reduce the electronics dead time, allowing for higher sustainable event rates in imaging applications

Within these limitations, the performance of the gamma camera (centroid position, FWHM measurements) are still in line with the requirements for its planned laboratory applications. For this prototype characterization, acquisition times longer than standard pre-clinical scan durations were employed, so the real performance in pre-clinical applications must be assessed in future studies. The results demonstrate that the prototype provides sufficient spatial resolving power for small-source imaging in the energy range relevant for ^{111}Ag.

4 Conclusion

This work presented the design, experimental characterization, and Monte Carlo validation of a compact gamma camera prototype developed for ^{111}Ag imaging in laboratory applications. The

2026 JINST 21 P10036

results demonstrate that a GAGG(Ce) scintillator coupled to a SiPM array and a tungsten collimator can be effectively used for the detection and imaging of the high-energy gamma emissions of this radionuclide, in particular the 342 keV line.

In the current configuration, based primarily on off-the-shelf components and a simplified calibration procedure, the prototype achieved a point-source spatial resolution of approximately 3 mm. The measured energy resolution, $\Delta E/E = 23.1\,\%$ at 342 keV, proved sufficient to enable photopeak selection and to suppress the Compton background for imaging applications. The comparison with Monte Carlo simulations showed consistency in both spectroscopic and spatial observables, supporting the validity of the adopted optical and electronic modeling. Preliminary tests on a mouse phantom indicate the possibility to determine the activity in different organs.

Future developments will focus on three main directions: first, the optimization of the collimator geometry for the ^{111}Ag energy spectrum, in order to improve the trade-off between detection efficiency and spatial resolution; second, the scaling of the system through a modular detector architecture, with the integration of a γ-ray shielding and the aim of increasing the active area and overall sensitivity; and third, the implementation of advanced statistical reconstruction methods, such as mean square estimation and super-resolution approaches, to mitigate light-sharing effects and improve spatial fidelity in configurations with mismatched pitches between collimator, scintillator, and photo-detector array.

In conclusion, the ISOLPHARM gamma camera prototype represents a proof of concept for the monitoring of ^{111}Ag uptake. The successful imaging of structured source configurations, including a multi-organ phantom, supports its potential as a dedicated instrument for future preclinical studies and radiopharmaceutical development.

Acknowledgments

The authors acknowledge the ISOLPHARM collaboration for the scientific discussions and support throughout the development of this work.

The authors are grateful to Andrea Fabbri (INFN-Sezione di Roma Tre) for his fundamental help in addressing numerous hardware-related issues associated with the experimental setup.

The authors also thank the Laboratorio Energia Nucleare Applicata (LENA) for providing access to the ^{111}Ag sources and for enabling the experimental measurements presented in this work.

The authors acknowledge the members of the Gamma-ray Astrophysics Laboratory at INAF-OAS Bologna for their continuous support, valuable assistance with code debugging, and help during the experimental activities.

The authors thank Bioemtech for the technical assistance provided throughout the system configuration and experimental phases of this study.

The authors acknowledge CAEN S.p.A. for providing the front-end electronics and for the continuous technical support during the development and operation of the experimental setup.

The authors acknowledge the use of AI-based software tools for code debugging and for the generation of some of the scientific illustrations included in this work.

References

[1] S.J. Goldsmith, *Targeted Radionuclide Therapy: A Historical and Personal Review*, *Semin. Nucl. Med.* **50** (2020) 87.

2026 JINST 21 P10036

[2] National Research Council (US) and Institute of Medicine (US) Committee on State of the Science of Nuclear Medicine, *Advancing Nuclear Medicine Through Innovation*, National Academies Press (2007) [DOI:10.17226/11985].

[3] A. Andrighetto et al., *The ISOLPHARM project: ISOL-based production of radionuclides for medical applications*, *J. Radioanal. Nucl. Chem.* **322** (2019) 73.

[4] INFN, *Isolpharm project*, https://isolpharm.pd.infn.it/?page_id=967.

[5] K. Van Audenhaege et al., *Review of SPECT collimator selection, optimization, and fabrication for clinical and preclinical imaging*, *Med. Phys.* **42** (2015) 4796.

[6] S.C. White and M.J. Pharoah, eds., *Oral Radiology: Principles and Interpretation*, 7 edition,, Mosby/Elsevier (2014).

[7] H. Ziessman, J. O'Malley, J. Thrall and F. Fahey, *Nuclear Medicine*, Fourth Edition, Elsevier (2014) [DOI:10.1016/c2010-0-65632-x].

[8] C. Wunderlich et al., *Large-Area SiPM Pixels (LASiPs) in SPECT*, 2022 *JINST* **17** C07021.

[9] G. Cozzi et al., *High-Resolution Gamma-Ray Spectroscopy With a SiPM-Based Detection Module for* 1″ *and* 2″ *$LaBr_3$:Ce Readout*, *IEEE Trans. Nucl. Sci.* **65** (2018) 645.

[10] D. Jenkins, *Novel scintillators and silicon photomultipliers for nuclear physics and applications*, *J. Phys. Conf. Ser.* **620** (2015) 012001.

[11] D. Renker and E. Lorenz, *Advances in solid state photon detectors*, 2009 *JINST* **4** P04004.

[12] P. Busca et al., *Experimental Evaluation of a SiPM-Based Scintillation Detector for MR-Compatible SPECT Systems*, *IEEE Trans. Nucl. Sci.* **62** (2015) 2122.

[13] S. David, M. Georgiou, E. Fysikopoulos and G. Loudos, *Evaluation of a SiPM array coupled to a $Gd_3Al_2Ga_3O_{12}$:Ce (GAGG:Ce) discrete scintillator*, *Phys. Med.* **31** (2015) 763.

[14] N. Otte, *The Silicon Photomultiplier: A New Device for High Energy Physics, Astroparticle Physics, Industrial and Medical Applications*, *eConf C* **0604032** (2006) 0018.

[15] J.Y. Yeom et al., *First Performance Results of Ce:GAGG Scintillation Crystals With Silicon Photomultipliers*, *IEEE Trans. Nucl. Sci.* **60** (2013) 988.

[16] Z. Yu et al., *Submillimeter Pixelated SPECT Detector Using GAGG:Ce and Light Guide With Optical Barrier Slits*, *IEEE Trans. Radiat. Plasma Med. Sci.* **9** (2025) 1015.

[17] R. Campana et al., *Measurement of the non-linearity in the γ-ray response of the GAGG:Ce inorganic scintillator*, *Nucl. Instrum. Meth. A* **1056** (2023) 168587 [arXiv:2308.06759].

[18] S. Xu, Z. Yan and Q. Wei, *A Survey of Crystals for SPECT Imaging*, *Crystals* **14** (2024) 1039.

[19] Q. Wei et al., *A side-by-side LYSO/GAGG phoswich detector aiming for SPECT imaging*, *Nucl. Instrum. Meth. A* **953** (2020) 163242.

[20] K. Nakanishi, S. Yamamoto and J. Kataoka, *Performance comparison of finely pixelated LYSO- and GAGG-based Si-PM gamma cameras for high resolution SPECT*, *Nucl. Instrum. Meth. A* **872** (2017) 107.

[21] S. Yamamoto, J. Kataoka, K. Kamada and A. Yoshikawa, *An ultrahigh spatial resolution radiation-imaging detector using 0.1 mm × 0.1 mm pixelated GAGG plate combined with 1 mm channel size Si-PM array*, *Nucl. Instrum. Meth. A* **919** (2019) 125.

[22] T. Fukuchi et al., *Beta-ray imaging system with γ-ray coincidence for multiple-tracer imaging*, *Med. Phys.* **47** (2020) 587.

[23] CAEN S.p.A., *A5202 — fers 64 channel readout unit*, https://www.caen.it/products/a5202.

2026 JINST 21 P10036

[24] Teledyne LeCroy, *T3DSO3000 Series Oscilloscopes*, https://www.teledynelecroy.com/oscilloscope/t3dso3000-series-oscilloscopes.

[25] Hamamatsu Photonics K.K., *S13361-3050AE-08 MPPC (SiPM) product page*, https://www.hamamatsu.com/eu/en/product/optical-sensors/mppc/mppc_mppc-array/S13361-3050AE-08.html.

[26] EPIC Crystal, *GAGG(Ce) Crystal product page*, https://www.epic-crystal.com/scintillation-crystals/gaggce-crystal.html.

[27] S. Kumar and T. Gupta, *A review of electrical discharge machining (EDM) and its optimization techniques*, *Mater. Today Proc.* (2023) in press.

[28] E. Technology, *EJ-560 Silicone Rubber Optical Interface*, https://eljentechnology.com/products/accessories/ej-560.

[29] CAEN S.p.A., *A5251 Header Adapter product page*, https://caen.it/products/a5251.

[30] CAEN S.p.A., *Janus Digital Multi-Channel Analyzer product page*, https://www.caen.it/products/janus/.

[31] J.-B. Cizel, *Citiroc 1A*, https://www.weeroc.com/read_out_chips/citiroc-1a/.

[32] CAEN S.p.A., *A5202*, https://www.caen.it/products/a5202/.

[33] M. Perri et al., *Amplitude Measurements With SiPM and ASIC (Citiroc 1A) Front-End Electronics*, *IEEE Trans. Nucl. Sci.* **70** (2023) 1023.

[34] D. Impiombato et al., *Characterization and performance of the ASIC (CITIROC) front-end of the ASTRI camera*, *Nucl. Instrum. Meth. A* **794** (2015) 185 [arXiv:1506.00264].

[35] M. Fang, S. Pani and A. Di Fulvio, *Enabling PSD-capability for a High-density Channel Imager*, in the proceedings of the *IEEE Nuclear Science Symposium (NSS) and Medical Imaging Conference (MIC) and 28th International Symposium on Room-Temperature Semiconductor Detectors*, Yokohama, Japan, 16–23 October 2021 [DOI:10.1109/NSS/MIC44867.2021.9875505] [arXiv:2204.13763].

[36] F. Garufi et al., *The Crystal Eye X and gamma-ray detector for space missions*, *J. Phys. Conf. Ser.* **2429** (2023) 012024.

[37] C.A. Kierans, *AMEGO: Exploring the Extreme Multimessenger Universe*, *Proc. SPIE Int. Soc. Opt. Eng.* **11444** (2020) 1144431 [arXiv:2101.03105].

[38] HERD collaboration, *The Plastic Scintillator Detector of the HERD space mission*, *PoS* **ICRC2021** (2021) 054.

[39] J. Fleury et al., *Petiroc and Citiroc: front-end ASICs for SiPM read-out and ToF applications*, 2014 *JINST* **9** C01049.

[40] Thorslab, *NPL41B laser*, https://www.thorlabs.com/item/NPL41B.

[41] Thorlabs Inc., *Nanosecond pulsed laser systems*, https://www.thorlabs.com/nanosecond-pulsed-laser-systems?tabName=Overview.

[42] D. Serafini, *Geant4 project for gamma camera*, https://github.com/dserafini/gamma-camera/.

[43] GEANT4 collaboration, *GEANT4 — A Simulation Toolkit*, *Nucl. Instrum. Meth. A* **506** (2003) 250.

[44] J. Allison et al., *Geant4 developments and applications*, *IEEE Trans. Nucl. Sci.* **53** (2006) 270.

[45] J. Allison et al., *Recent developments in Geant4*, *Nucl. Instrum. Meth. A* **835** (2016) 186.

[46] D. Serafini et al., *Monte Carlo simulation of the ISOLPHARM gamma camera for Ag-111 imaging*, 2026 *JINST* **21** C04037 [arXiv:2502.20112].

2026 JINST 21 P10036

[47] Gigahertz-Optik GmbH, *ODP97*, https://www.gigahertz-optik.com/en-us/product/odp97/.

[48] R. Pani et al., *Position algorithm for monolithic scintillation crystals based on charge projection readout*, 2016 *JINST* **11** C01061.

[49] Z. Deng, Y. Deng and G. Chen, *Design and Evaluation of LYSO/SiPM LIGHTENING PET Detector with DTI Sampling Method*, *Sensors* **20** (2020) 5820.

[50] Eckert & Ziegler, *Barium-133 Radionuclide Data Sheet*, Eckert & Ziegler Isotope Products (2023).

[51] BIOEMTECH, *Phantoms*, https://bioemtech.com/product/phantom/.

[52] B. Dogdas, D. Stout, A.F. Chatziioannou and R.M. Leahy, *Digimouse: a 3D whole body mouse atlas from CT and cryosection data*, *Phys. Med. Biol.* **52** (2007) 577.

[53] A. Fabbri et al., *A new iterative algorithm for pixilated and continuous scintillating crystal*, *Nucl. Instrum. Meth. A* **648** (2011) S79.

[54] M. Kawulok et al., *Deep Learning for Multiple-Image Super-Resolution*, *IEEE Geosci. Remote Sens. Lett.* **17** (2020) 1062.

[55] M. Morrocchi et al., *A detector module composed of pixellated crystals coupled to SiPM strips*, 2014 *JINST* **9** P08007.

2026 JINST 21 P10036